International Journal of Mining Science and Technology 32 (2022) 225–236

Contents lists available at ScienceDirect

International Journal of Mining Science and Technology

journal homepage: www.elsevier.com/locate/ijmst

Dynamic analysis of heat extraction rate by supercritical carbon dioxide in fractured rock mass based on a thermal-hydraulic-mechanics coupled model

Chunguang Wang [a,*], Xingkai Shi [a], Wei Zhang [a,b], Derek Elsworth [c], Guanglei Cui [d], Shuqing Liu [a], Hongxu Wang [a], Weiqiang Song [a], Songtao Hu [e], Peng Zheng [f]

[a] College of Energy and Mining Engineering, Shandong University of Science and Technology, Qingdao 266590, China
[b] New-energy Development Center of Sinopec Shengli Oilfield, Dongying 257001, China
[c] Energy and Mineral Engineering and G3 Center, Penn State University, University Park, PA 16802, USA
[d] Key Laboratory of Ministry of Education on Safe Mining of Deep Metal Mines, Northeastern University, Shenyang 110004, China
[e] Shandong Provincial Geo-Mineral Engineering Co., Ltd, Jinan 250013, China
[f] Qingdao Wofu New Energy Science and Technology Co., Ltd, Qingdao 266010, China

ARTICLE INFO

Article history:
Received 9 October 2021
Received in revised form 2 November 2021
Accepted 15 December 2021
Available online 24 December 2021

Keywords:
Supercritical CO_2
Heat extraction
Hot rock
Geothermal energy
Fracture-matrix interaction

ABSTRACT

Heat production from geothermal reservoirs is a typical heat transfer process involving a cold working fluid contacting a hot rock formation. Compared to the thermal-physical characteristics of water, supercritical CO_2 ($scCO_2$) has a higher heat storage capacity over a wide temperature-pressure range and may be favored as a heat transfer fluid. Singularly characteristic of $scCO_2$-based heat extraction is that the hydraulic-thermal properties of the $scCO_2$ vary dramatically and dynamically with the spatial pressure gradient during unsteady-state flow along fracture. This highly nonlinear behavior presents a challenge in the accurate estimation of heat extraction efficiency in $scCO_2$-based EGS. In this paper, a thermal–hydraulic-mechanical (THM) coupled model is developed by considering deformation of the fractured reservoir, non-Darcy flow and the varying thermal-physical properties of $scCO_2$. The proposed model is validated by matching the modeling temperature distribution with published data. The results show that during continuous injection of $scCO_2$, the fracture first widens and then narrows, ultimately reopening over the long term. The sequential fracture deformation behaviors are in response to the combined impacts of mechanical compression and thermally-induced deformation. By controlling the injection parameters of the $scCO_2$, it is found that the heat extraction rate is positively correlated to its pore pressure or mass flow rate. The heat extraction rate can be significantly enhanced, when the inlet temperature of $scCO_2$ is below its critical temperature. As a result, the heat increment recovered per unit mass of $scCO_2$ decreases as the hot rock is gradually cooled. Meanwhile, the heat increment recovered per unit mass of $scCO_2$ decreases by increasing the inlet temperature of $scCO_2$ or its mass flow rate, but increases as the outlet pressure rises. Furthermore, multi-linear regression indicates that controlling the inlet temperature of the $scCO_2$ can significantly improve the thermodynamic efficiency of heat extraction.

1. Introduction

Accessing geothermal resources remains one of the most promising alternatives to provide plentiful and clean energy [1-3]. As a type of geothermal reservoir, hot dry rock (HDR) has received extensive attention due to its vast reserves [4,5]. An HDR reservoir is typically a low-permeability but high-temperature rock formation, whose commercial geothermal exploitation requires permeability enhancement by stimulation to be viable [6,7]. Heat extraction from enhanced geothermal systems (EGS), represents a re-branding of HDR and is completed by injecting a low-temperature working fluid into natural or artificial hydraulic fractures, and then relying on heat exchange from the fractured rock matrix to further increase fluid transmission [8,9]. Compared to H_2O-based working fluids, supercritical CO_2 ($scCO_2$) has a higher density to viscosity ratio, exerts a larger buoyant force that can reduce parasitic losses and zero/low salinity [10]. Some characterizations of $scCO_2$-based EGS projects demonstrate that the heat extraction rate can be as high as 160% that of

* Corresponding author.
E-mail address: cgwang@sdust.edu.cn (C. Wang).

https://doi.org/10.1016/j.ijmst.2021.12.004
2095-2686/

H_2O-based EGS [11]. A comprehensive understanding of heat transfer process between the working fluid and the HDR reservoir is crucial in predicting long-term heat production and operational life of the EGS.

Flow-through experiments using CO_2 or water show that the heat extraction rate can increase with flow rate [12] and fluid pressure [13,14], but decrease with fracture tortuosity. As a key parameter in the prediction of heat extraction rate (HE rate) [15,16], the heat transfer coefficient (HTC) is an empirical index representing the interaction between the hydrodynamics of fluid motion and solid surface geometry [15,17]. The HTC is positively correlated with flow rate, but negatively with fracture aperture [18-23]. Compared to smooth parallel-plate fractures, the impacts of fracture roughness on the variation of HTC remain equivocal [12,20,23–34]. In addition, an ill-defined temperature distribution along the rough fracture surface results in inadequate constraint of the heat extraction rate. This is because fracture roughness may disturb uniform laminar flow, in which the redistribution of fluid flow velocity will alter the spatial distribution of temperature. In this case, the thermal conductivity of $scCO_2$ is dependent of the active combined temperature–pressure conditions, whereby for water, it is primarily controlled by temperature alone. The modeling of heat extraction is challenged by the effects of thermal–hydraulic-mechanics (THM) [26-34].

Heat recovery from hot fractured rock necessitates the mean cooling of the reservoir. This can cause fractures/joints to deform due to the cooling-induced shrinkage of the solid volume together with the complex impacts of fluid overpressures and mineral dissolution or pressure solution [35-44]. If the evaluation of HDR reservoirs ignores the thermal–mechanical coupling effects, the production temperature will decrease at a slower rate compared to when THM coupling is incorporated [45,46]. Spatio-temporal distributions of both thermal and effective stresses impact fracture porosity and can generate non-uniform fluid flow [47-49]. Where the thermal disturbance among multiple-parallel fractures is considered, larger fracture spacing weakens the thermal interaction among fractures [33]. Thus, an optimal fracture spacing, ranging between 30 and 90 m, may be defined to maximize the lifetime of a fractured reservoir [50]. In this case, heat transfer behavior within individual fractures can proceed independently-and the multiple-fracture model then degenerates into a single fracture model. It is notable that thermophysical properties of CO_2 are sensitive to the thermal–hydraulic state of the EGS, especially close to the critical point or pseudo-critical point of CO_2. When hot rock is gradually cooled, increasing CO_2 density can significantly retard the flow velocity, consequently impacting its specific heat capacity and thermal conductivity [51]. Although heat transfer to and within $scCO_2$ has been extensively described by prior models [52-54], less consideration has been given to the optimum heat extraction rate considering the dynamic and nonlinear evolution of the thermophysical properties of the $scCO_2$ coupled with the THM response of the reservoir.

In this study, we explore heat extraction sensitivity of HDR reservoirs to the thermophysical properties of $scCO_2$ by developing a thermal–hydraulic-mechanical (THM) coupled model, which can couple three-dimensional rock deformation with the non-Darcy flow of $scCO_2$. In particular, the thermophysical evolution of the CO_2 is governed by the Span and Wagner model [55]. The fractured region within the hot rock is defined as an equivalent porous medium, where the assumption of local thermal equilibrium between facture surface and matrix is applied. The proposed numerical model is validated by comparing with published experimental results. A series of sensitivity analysis under various injection conditions are evaluated by comparing heat increments with the outlet temperatures of the $scCO_2$. This work provides insights in determining maximum efficiency of such novel systems.

2. Mathematical model

In the following, the proposed fully coupled thermal-hydro-mechanical model is governed by the elastic deformation and stress equilibrium of the solid, together with conservation of fluid mass and energy for the non-isothermal fluid-solid system. A tortuous, fluid-transmitting fracture is defined as an equivalent porous medium, as shown in Fig. 1. The ultra-low-permeability rock matrix is isotropic and homogeneous, accommodating negligible flux of the working fluid. In the absence of water, chemical reactions between the anhydrous $scCO_2$ and minerals are also neglected.

2.1. Governing equation of fluid flow within a fracture

The governing equation for fluid flow within the fracture is defined by mass conservation as:

$$\varphi\frac{\partial\rho}{\partial t}+\rho\frac{\partial\varphi}{\partial t}+\nabla\cdot(\rho\mathbf{v})=Q \tag{1}$$

where ρ is the fluid density; Q the mass source per unit volume per unit time; p the fluid pressure; φ the porosity; and $\mathbf{v}$ the velocity vector for the fluid.

The Reynolds number is defined as:

$$Re=\frac{\rho\mathbf{v}l}{\mu}=\frac{2M}{W\mu} \tag{2}$$

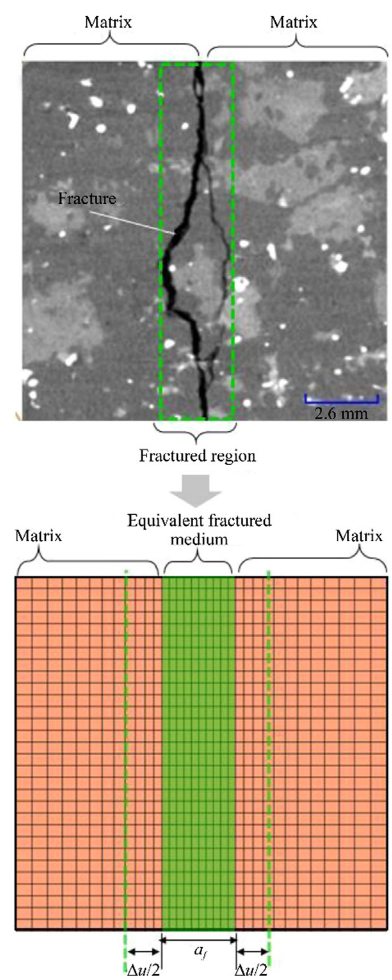

Fig. 1. Schematic of an equivalent fractured medium (modified from a CT image of fractured rock [56]).

where l is the characteristic length of the fluid pathway; μ the fluid viscosity; M the mass flow rate; and W the fracture aperture. According to initial values of the parameters above listed in Table 1, the Reynolds number for CO_2 typically exceeds that for laminar flow and the application of the standard from of Darcy's law (1–10). Thus the flow equation for $scCO_2$ is governed by the Forchheimer model.

$$\nabla p = -\frac{\mu}{k}\mathbf{v} - \frac{c_{\mathrm{F}}}{\sqrt{k}}\rho \mathbf{v}^2 \tag{3}$$

where ∇p is the pressure gradient; μ the fluid viscosity; k the permeability; and c_{F} the Forchheimer parameter.

The dilation/compaction of the fracture zone embedded in the equivalent fractured medium is represented as:

$$\Delta a_{\mathrm{e}} = u_z|_{z=a_{\mathrm{f}}/2} - u_z|_{z=-a_{\mathrm{f}}/2} \tag{4}$$

where $u_{z|z=}a_{\mathrm{f}}/2$ and $u_z|_{z=}$-$a_{\mathrm{f}}/2$ are displacements across of the equivalent fracture zone.

According to the definition of porosity (ratio of void volume V_{p} to bulk volume V_{f}), the porosity of the equivalent fracture is defined as:

$$\varphi = \frac{V_{\mathrm{p}}}{V_{\mathrm{f}}} = \frac{a_{\mathrm{e}}}{a_{\mathrm{f}}} \tag{5}$$

where a_{e} is the hydraulic aperture of the equivalent fracture; and a_{f} the void volume between the two fracture surfaces.

Permeability of the equivalent fracture is defined as [57]:

$$k = \frac{a_{\mathrm{e}}^2}{12} \tag{6}$$

2.2. Constitutive equation for fractured rock

The Navier-type constitutive equations for the fracture and the matrix are expressed as [58,59]

$$G_{\mathrm{m}} u_{i,kk} + \frac{G_{\mathrm{m}}}{1-2\mu} u_{k,ki} - 3K_{\mathrm{m}}\alpha_{\mathrm{T}}\Delta T_i + f_i = 0 \text{ for the rock matrix} \tag{7}$$

$$G_{\mathrm{f}} u_{i,kk} + \frac{G_{\mathrm{f}}}{1-2\mu} u_{k,ki} - p - 3K_{\mathrm{f}}\alpha_{\mathrm{T}}\Delta T_i + f_i = 0 \quad \text{for the rock fracture} \tag{8}$$

where G and μ are the shear modulus and Poisson ratio respectively; K the bulk modulus; α_{T} the linear thermal expansion coefficient; p the fluid pressure; and u_{ij} the displacement component. The subscripts m and f represent matrix and fracture, respectively.

2.3. Heat transfer equation

Heat transfer only occurs within the rock matrix, where energy conservation is governed by Fourier's Law as:

$$\rho_{\mathrm{r}} c_{\mathrm{pr}} \frac{\partial T}{\partial t} - \nabla \cdot (\lambda_{\mathrm{r}} \nabla T) = Q_{\mathrm{h}} \tag{9}$$

where λ is the thermal conductivity; ρ_{r} the density of the rock; c_{pr} the specific heat capacity of the rock; and Q_{h} the heat source.

Local thermal equilibrium between the equivalent fracture and the matrix is assumed. Cooling by the working fluid within the hot fracture recovers heat by conduction and removes it by convection. Relevant parameters are obtained by volume averaging the solid–fluid properties in the fractured region. The energy conservation equation is rewritten as:

$$(\rho c_p)_{\mathrm{eff}} \frac{\partial T}{\partial t} - \nabla \cdot (\lambda_{\mathrm{eff}} \nabla T) + \rho_{\mathrm{l}} c_{p\mathrm{l}} v \cdot \nabla T = Q_{\mathrm{h}} \tag{10}$$

where ρ_{l} is the fluid density; $c_{p\mathrm{l}}$ the specific heat at constant pressure of the fluid; and λ_{l} the thermal conductivity of the fluid; $(\rho c_p)_{\mathrm{eff}} = (1-\varphi)\rho_{\mathrm{r}} c_{\mathrm{pr}} + \varphi \rho_{\mathrm{l}} c_{\mathrm{pl}}$; and $\lambda_{\mathrm{eff}} = (1-\varphi)\lambda_{\mathrm{r}} + \varphi\lambda_{\mathrm{l}}$ [60].

2.4. Thermal-physical properties of $scCO_2$

Thermal-physical properties of $scCO_2$ include specific heat capacity, density, dynamic viscosity and thermal conductivity. The thermal-physical equation defining the temperature and pressure dependence for $scCO_2$ is adopted from the Span and Wagner model [55]. Since the accuracy of the Span and Wagner over a broad range of temperatures and pressures is widely accepted, this model is also used by the National Institute of Standards and Technology, USA [61]. The state equation for CO_2 is defined as a function of the dimensionless Helmholtz energy:

$$\Phi(\delta,\tau) = \Phi^0(\delta,\tau) + \Phi^{\mathrm{r}}(\delta,\tau) \tag{11}$$

where Φ and Φ^{r} are the behavior of an ideal gas and the residual gas, respectively; $\delta = \rho/\rho_{\mathrm{c}}$ the reduced density representing the ratio of fluid density to critical density; and $\tau = T/T_{\mathrm{c}}$ the inverse reduced temperature, representing the ratio of the critical temperature of the fluid to the actual temperature. CO_2 density can then be rewritten as:

$$\rho = \frac{P(\delta,\tau)}{RT(1+\delta\Phi_{\delta}^{\mathrm{r}})} \tag{12}$$

where $P(\delta,\tau)$ is the fluid pressure; $\Phi_{\delta}^{\mathrm{r}}$ the partial derivative of Φ^{r} to δ; and R the specific gas constant as 0.1889 kJ/(kg·K).

The specific heat capacity of CO_2 at constant pressure is then expressed as:

$$\frac{c_p}{R} = -\tau^2\left(\Phi_{\tau\tau}^0 + \Phi_{\tau\tau}^{\mathrm{r}}\right) + \frac{\left(1+\delta\Phi_{\delta}^{\mathrm{r}} - \delta\tau\Phi_{\delta\tau}^{\mathrm{r}}\right)^2}{1+2\delta\Phi_{\delta}^{\mathrm{r}} + \delta^2\Phi_{\delta\delta}^{\mathrm{r}}} \tag{13}$$

where $\Phi_{\tau\tau}^{\mathrm{r}} = \frac{\partial^2\Phi}{\partial\tau^2}$; $\Phi_{\delta\delta}^{\mathrm{r}} = \frac{\partial^2\Phi}{\partial\delta^2}$; and $\Phi_{\delta\tau}^{\mathrm{r}} = \frac{\partial^2\Phi}{\partial\delta\partial\tau}$.

Both the viscosity and thermal conductivity of CO_2 transport are represented by the Vessovic-Fenghour model [62,63] as:

$$X(\rho,T) = X_0(T) + \Delta X(\rho,T) + \Delta X_{\mathrm{c}}(\rho,T) \tag{14}$$

where $X(\rho,T)$ represents a specific property of the CO_2; $X_0(T)$ the transport property under the zero-density state; $\Delta X(\rho,T)$ the excess transport property of the fluid; and $\Delta X_{\mathrm{c}}(\rho,T)$ the critical enhancement due to changes in temperature and pressure near the critical point. The phase transition of CO_2 is recovered from Newton-

Table 1
Parameters used for model validation [64,65].

Variable	Parameter	Value	Variable	Parameter	Value
p_0	Initial fluid pressure	8.1 (MPa)	p_{out}	Outlet pressure	8.1 (MPa)
T_0	Initial temperature	80 (℃)	P_{c}	Confining pressure	10.1 (MPa)
M_{in}	Inlet mass flow	0.35 (kg/h)	ρ_{ga}	Density of granite	2584 (kg/m^3)
α_{T}	Thermal expansion coefficient	6×10^6 (1/K)	E	Young's modulus of granite	40 (GPa)
λ_{m}	Thermal conductivity coefficient	2.45 (W/(m·K))	μ	Poisson's ratio of granite	0.25
c_{pm}	The specific heat capacity of granite	1100 (J/(kg/K))	a_{e}	Hydraulic aperture	0.2 (mm)

Raphson iteration. Modeling temperature-dependent -physical parameters of CO_2 (including density, specific heat capacity, viscosity and thermal conductivity) are shown in Fig. 2, respectively.

2.5. Cross-couplings

Fig. 3 is a schematic of the cross-couplings among the various multi-physical processes. Injection of cold $scCO_2$ not only changes the hydraulic conditions within the fracture, but also extracts heat from the surrounding hot rock by conduction. As a consequence, heat transfer within the rock can drive out-of-step thermal deformations between the fracture and matrix, while varying hydraulic condition will affect CO_2 mas flow and the heat extraction rate from the fracture-matrix interface.

3. Model analysis

We validate the proposed THM model against a set of published experimental data [64]. This particular experimental observation investigated the effects of convective heat transfer of $scCO_2$ by measuring the temperature variation within a fractured granite core with 25 mm-radius and 50 mm-length. Fig. 4 shows the 3D geometry of the granite core, where a throughgoing fracture has an aperture of 0.2 mm and a width of 40 mm.

(1) Mechanical boundary conditions

A confining pressure is applied on the circumferential surface of the rock sample,

$$p = p_c \tag{15}$$

Displacements at the two ends of the model are fixed as:

$$u_x|_{x=0} = u_x|_{x=l} = 0 \tag{16}$$

(2) Thermal boundary conditions

Given that the periphery of the holder was heated by an electric heating jacket, heat conduction within the oil bath, gasket and metal end-caps must be considered. The inflow condition into the fracture is given as:

$$-\mathbf{n}\cdot\mathbf{q} = \rho\Delta H\mathbf{u}\cdot\mathbf{n}\,\Delta H = \int_{T_{in}}^{T} c_p \mathrm{d}T \tag{17}$$

where T_{in} is the inlet temperature of the CO_2; q the net rate of heat loss; u the flow velocity with n defining the unit normal vector.

The outer surface of the calculation model, excepting the fracture inlet, is thermally insulated and defined as a null heat flow boundary condition as:

$$-\mathbf{n}\cdot\mathbf{q} = 0 \tag{18}$$

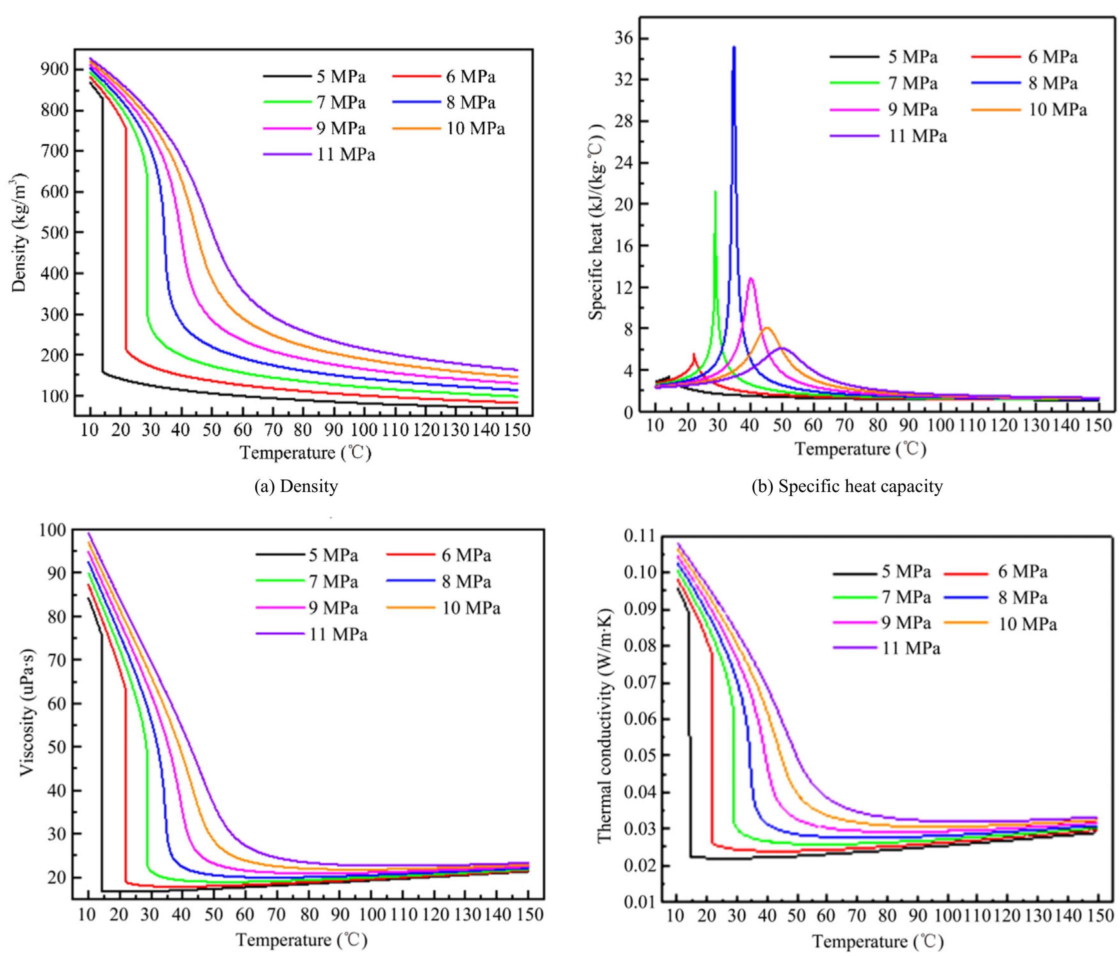

(a) Density (b) Specific heat capacity (c) Viscosity (d) Thermal conductivity

Fig. 2. Modeling temperature-dependent CO_2 parameters using the Span and Wagner model [55].

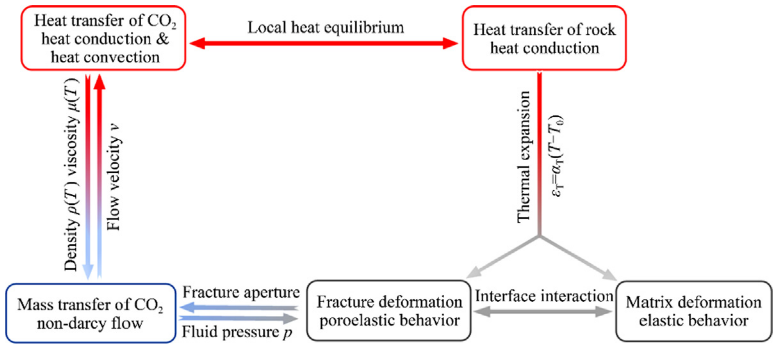

Fig. 3. Schematic of cross-couplings among multi-physical processes.

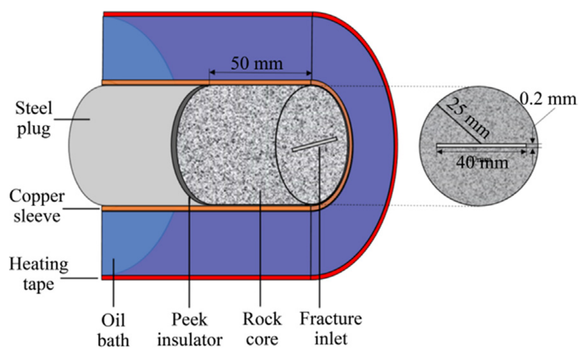

Fig. 4. Geometry of the benchmark experimental model including the rock core and holder [64].

(3) The flow boundary conditions

A mass flow condition for the inlet of the rock is given as:

$$-\int_{d\Omega} n\rho u dS = M_0 \tag{19}$$

where S is the cross-sectional area of the fracture; and M_0 the mass flow rate of the injected CO_2. Finally, the pressure is defined at the outlet of the fracture as:

$$p = p_{out} \tag{20}$$

3.1. Model validation

Numerical solutions to these field equations are recovered from COMSOL multiphysics. Relevant material parameters are listed in Table 1. The temperature distribution at the fracture wall is recovered along the axis of the cylindrical sample. Fig. 5a plots locations of temperature measurement points. It should be noted that the injected fluid is preheated in the holder, prior to flowing into the rock. The temperature of the injected fluid is a function of time, $T_{in} = T_{inj}(t)$, according to linear interpolation from the experimental data. Fig. 5b compares the measured temperature data against the modeling results. It is clear that the modeling temperature-time distribution along the rock is in good agreement with the measured temperature data (with R-Squared values > 95%).

3.2. Fracture aperture change induced by CO_2 cooling

In this section, we evaluate the spatial and temporal variation of heat transfer in the $scCO_2$-rock system at sub-prototype scale by expanding the size of the numerical model. The diameter of the modified model is expanded from 50 to 1000 mm, and its length increases from 50 to 500 mm, as shown in Fig. 6. The overall width of the fracture region increases to 300 mm, but its hydraulic aperture remains unchanged (retained at 0.2 mm). The boundary conditions for fluid flow and solid deformation are identical to those for Section 3. A constant temperature of 150 °C is applied on the outer boundary. Material parameters are as listed in Table 2.

Considering that the fracture aperture change is related to the hydraulic-thermal gradients, Fig. 7a shows the time-dependent fracture aperture variation with respect to THM-induced strains at the central point of the fracture domain. In the first 20 s (Stage I), the fracture aperture initially widens as a result of the $scCO_2$ injection. During this stage, the pore pressure-dependent strain rapidly increases, while both the thermally-induced fracture strain and matrix-induced strain remain unchanged. This indicates that the influent CO_2 is rapidly heated to the initial temperature of the hot rock, during which time both the thermal strains across the fracture and within the rock matrix are negligible. From 20 to 5000 s approximately (Stage II), the fracture aperture begins to slightly reduce as a result of the continuing CO_2 inflow. This is attributable to the cooling shrinkage of the matrix adjacent to the inlet. Beyond 5000 s (Stage III), the fracture aperture increases gradually. During this process, although the effect of cooling shrinkage can reduce the fracture strain to some extent, the volume shrinkage of the rock matrix dominates over the increase in fracture aperture.

Fig. 7b compares spatial variations of thermal properties of CO_2 resulting from only considering the doublet of TH-coupling relative to the full triplet of THM-coupling. It is clear from this that both the specific heat and density of the CO_2 are insensitive to changes in the fracture aperture. However, the CO_2 flow velocity for the full triplet of THM-coupling is higher than that for the TH-only case, contrary to the equivalent thermal conductivity, as shown in Fig. 7c. This indicates that the mechanical compression effects have little impact on the thermal-physical properties of CO_2, but can significantly change volume flow rate of CO_2 and resultant heat conduction capacity.

4. Multi-factor evaluations of heat extraction by CO_2

Since the thermodynamic properties of CO_2 are sensitive to both pressure and temperature, the outlet temperature of CO_2 alone cannot define the heat extracted over the entire pathway of circulation. Rather, the heat extraction rate of $scCO_2$ must be recovered from the enthalpy differential between outlet and inlet [67]:

$$P = M_{out}(H_{out} - H_{in}) \tag{21}$$

where P is the heat extraction rate; M_{out} the CO_2 mass flow rate at the outlet (steady flow); H_{in} and H_{out} the specific enthalpies at the inlet and outlet, respectively defined in terms of internal energy per unit mass, $\breve{u}$, and pressure, p, as $H=\breve{u}+p/\rho$. Both production tem-

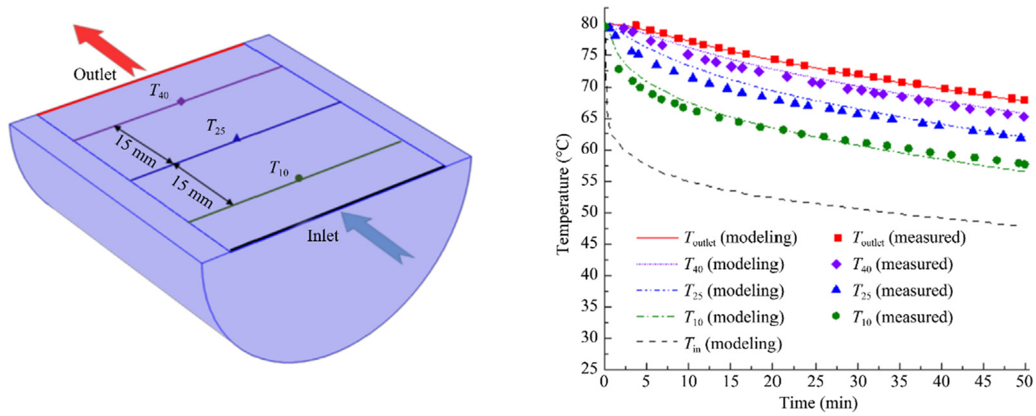

(a) Semi-cylinder of 3D model

(b) Comparison of modeling temperature values with published experimental data

Fig. 5. Benchmark model validation from the matching of modeling data with the published data.

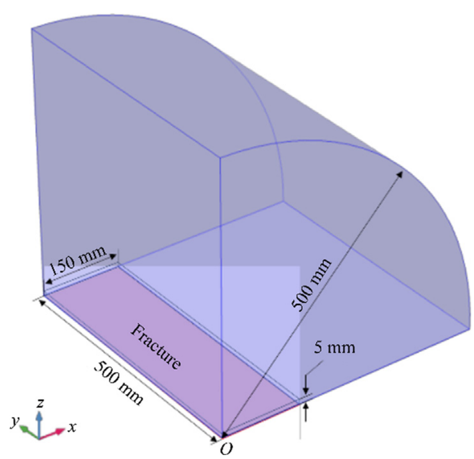

Fig. 6. Quarter geometry of the sized-increasing 3D model.

perature and the heat extraction rate are explored in light of three contrasting scenarios where controls are placed sequentially on inlet temperature and outlet pressure, both represented in the enthalpy differential, and the mass flow rate [68,69]. Fig. 8 shows schematically how each of these three individual scenarios affects heat extraction rate by the CO_2. When the controls on CO_2 injection are defined, a complex chain of interactions among the thermodynamic properties of CO_2 plays an important role in controlling $scCO_2$ flow and its heat storage capacity. This implies that one injection process/constraint affects two or more thermodynamic properties of the resulting CO_2 flow and therefore defines the change in specific enthalpy of the recovered fluid.

4.1. Scenario I: Effect of initial inlet temperature on heat extraction rate

The inlet temperature of the CO_2 is varied across the range 25–50 ℃ in increments of 5 ℃. All injection mass flow rates are 0.25 g/s, in which case effluent CO_2 pressure is held at 9 MPa under the various temperature conditions. Fig. 9 shows the heat extraction profiles with increasing initial temperatures of the influent CO_2. The parametric analysis indicates that the outlet temperature of the CO_2 is positively correlated with the initial temperature of the CO_2. However, injecting cooler CO_2 elevates the heat extraction rate as the temperature differential is larger. From Fig. 2a, the specific heat capacity of CO_2 under a specific pressure peaks at a critical temperature. It is apparent from Fig. 9b that the area enveloped by the specific heat to temperature relation reduces as the initial temperature increases. This indicates that the heat extraction capacity of CO_2 can be significantly increased if the initial temperature of the CO_2 is lower than the temperature corresponding to the peak in specific heat.

4.2. Scenario II: Effect of CO_2 pressure on heat extraction rate

Since fluid flow rate is controlled by pressure gradient, the CO_2 pressure along the entire fracture can be held constant by retaining the injection mass flow rate of CO_2 constant together with the outlet pressure. The pressure-dependent outlet temperature and heat extraction rates of $scCO_2$ are shown in Fig. 10a. The profiles of the effluent CO_2 temperature *vs* time in Fig. 10a indicate that the injected CO_2 is rapidly heated to 150 °C and then maintains this for 1200 s followed by a slow decline to an equilibrium profile. The higher the outlet pressure is the lower the temperature of the effluent CO_2 is. This result indicates that although the first outflow of CO_2 under a set pressure can be fully heated by the hot rock, the following outflow of CO_2 cools

Table 2
Parameters for modeling of the up-scaled prototype model [64,66].

Variable	Parameter	Value	Variable	Parameter	Value
E_m	Young's modulus of matrix	40 (GPa)	μ	Poisson's ratio of granite	0.25
E_f	Young's modulus of fracture	0.5 (GPa)	λ_m	thermal conductivity of granite	2.45 (W/(m · K))
c_{pm}	The specific heat capacity of granite	1100 (J/(kg/K))	ρ_r	Density of granite	2584 (kg/m^3)
α_T	Thermal expansion coefficient	6×10^6 (1/K)	a_e	Hydraulic aperture	0.2 (mm)
p_{out}	Outlet pressure	9 (MPa)	M_{in}	Injected mass flow rate	0. 25 (g/s)
P_c	Confining pressure	20 (MPa)	T_{in}	The inlet temperature	50 (℃)
T_0	The initial temperature	150 (℃)	p_0	Initial fluid pressure	0.101 (MPa)

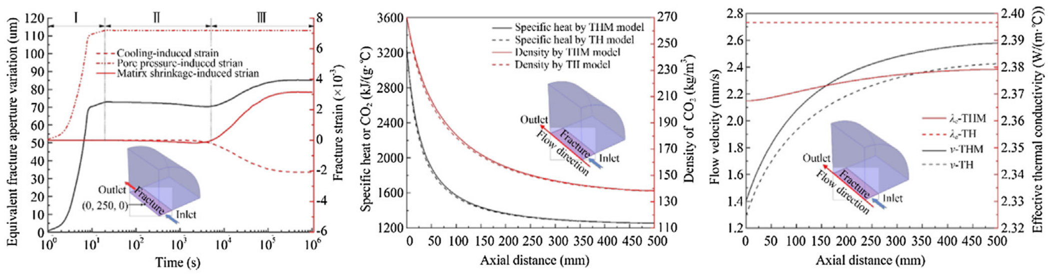

(a) Aperture change at central point of the fracture path

(b) Spatial changes of specific heat and density of CO_2 along flow pathway

(c) Spatial changes of flow rate and thermal conductivity of CO_2

Fig. 7. Spatio-temporal variations in heat transfer within the CO_2-rock system.

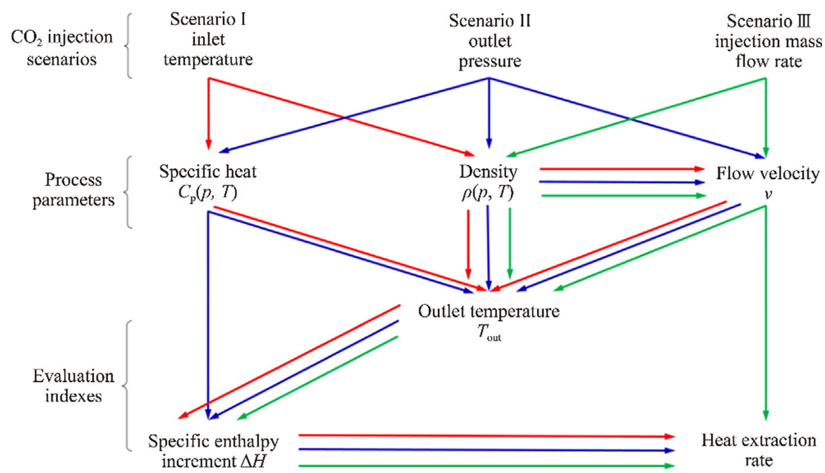

Fig. 8. Schematic diagram of nonlinear interactions among heat transfer process using different controlling scenarios.

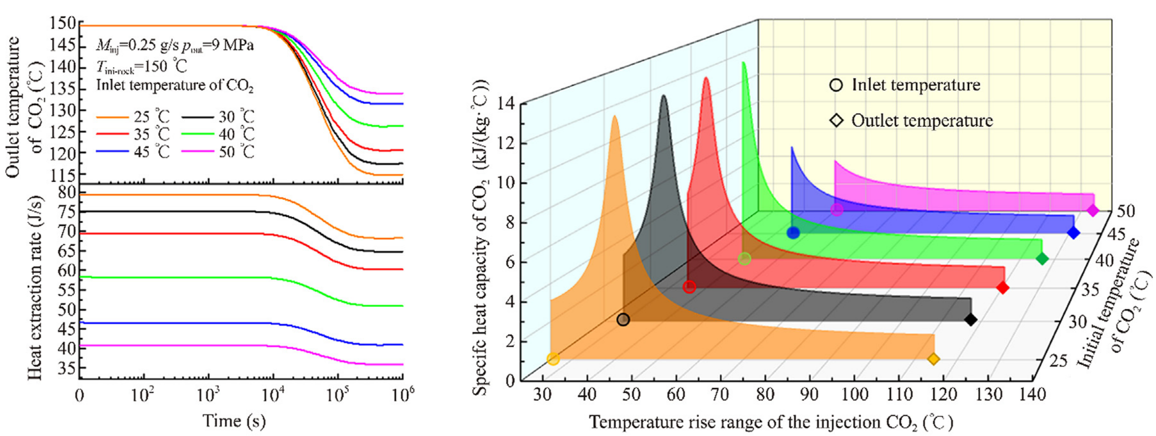

(a) Variation of outlet temperature and heat extraction rate with time

(b) Specific heat capacity profiles of CO_2 under different temperature ranges

Fig. 9. Modeled specific heat capacity profiles resulting from various controls on inlet temperature conditions.

as the heat supply from the rock diminishes. Relevant heat extraction rates of CO_2 under different outlet pressures are shown in Fig. 10a. During the $scCO_2$ flooding, the heat extraction rate at the outlet is initially maintained but then falls to a steady state. Different from the changes in temperature of the effluent CO_2, the heat extraction rate increases with a rise in outlet pressure when the mass flow rate is fixed. In order to interpret the mechanism controlling the heat extraction rate for the $scCO_2$, Fig. 10b shows the distribution profiles of the outlet flow rate and specific heat of $scCO_2$ along the fracture when the effluent $scCO_2$ reaches an equilibrium state. Increasing outlet pressure of the CO_2 reduces the fluid flow rate but enhances the specific heat of the CO_2. These changes can explain the reduction in the outlet temperature of CO_2 with an increase in fluid pressure. Given that the mass flow rate is set at 0.25 g/s, increasing fluid pressure can raise both the density and viscosity of the CO_2, resulting in a reduction in the rate of CO_2 transport. In this case, both the higher heat storage capacity (specific heat) and lower

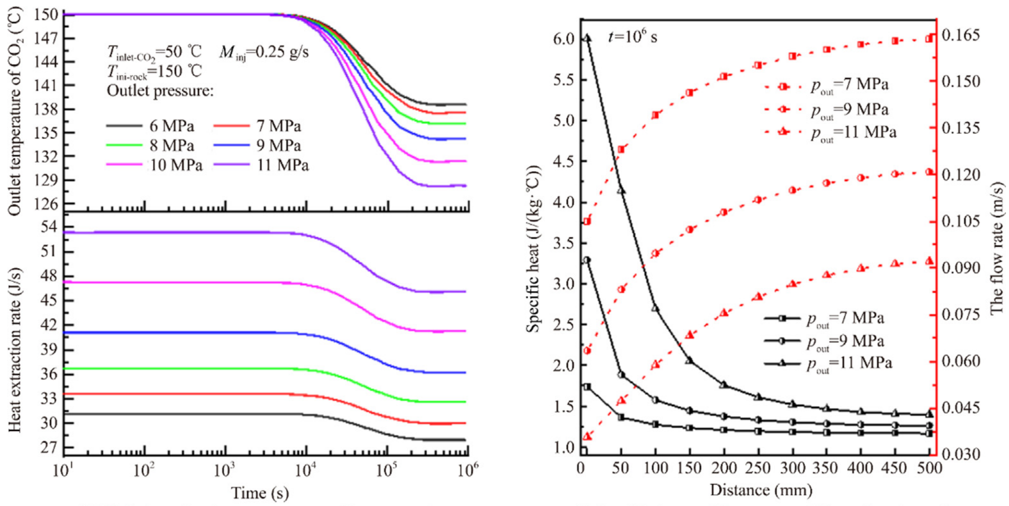

(a) Variation of outlet temperature and heat extraction rate with time

(b) Specific heat and flow rate at different locations of the fracture in equilibrium state

Fig. 10. Modeling results for different pressure conditions.

flow velocity can be beneficial in the recovery of heat from the hot rock. It should be noted that outlet temperature is reduced by the rise in the specific heat of CO_2 and increased by the reduction in CO_2 flow rate. It can be demonstrated from the drop in outlet temperature that the specific heat of the CO_2 can dominate the process of heat extraction.

4.3. Scenario III: Effect of mass flow rate on heat extraction

Heat recovery by $scCO_2$ is examined by increasing mass rates of injection from 0.15 to 0.3 g/s, in increments of 0.05 g/s. As shown in Fig. 11a, increasing the mass flow rates reduces the outlet temperature in the long-term but increases the net heat extraction rate. Considering that the evolution of the heat extraction rate with time is closely related to the temperature reduction in the effluent CO_2, we calculate the specific enthalpy increment and average density of injection over different durations of the heat transfer ($t = 10^2$ s, $t = 3 \times 10^4$ s and $t = 10^6$ s). As shown in Fig. 11b, at the beginning of the CO_2 injection (corresponding to a time of 10^2 s), the specific enthalpy increments of $scCO_2$ are maintained at 163 J/kg and are insensitive to changes in the mass flow rate. This is because the influent CO_2 can be heated to the initial temperature of the granite. As a result, the heat extraction rate is positively related to the mass flow rate of CO_2. As a result of the continuing heat transfer between the granite and CO_2, the matrix temperature around the fracture begins to gradually drop. The specific enthalpy increments of $scCO_2$ reduce with an increase in the mass flow rate. When the effluent CO_2 reaches an equilibrium temperature, the specific enthalpy increment reduces linearly from 157 to 138 J/kg as the mass flow rate increases from 0.1 to 0.3 g/s.

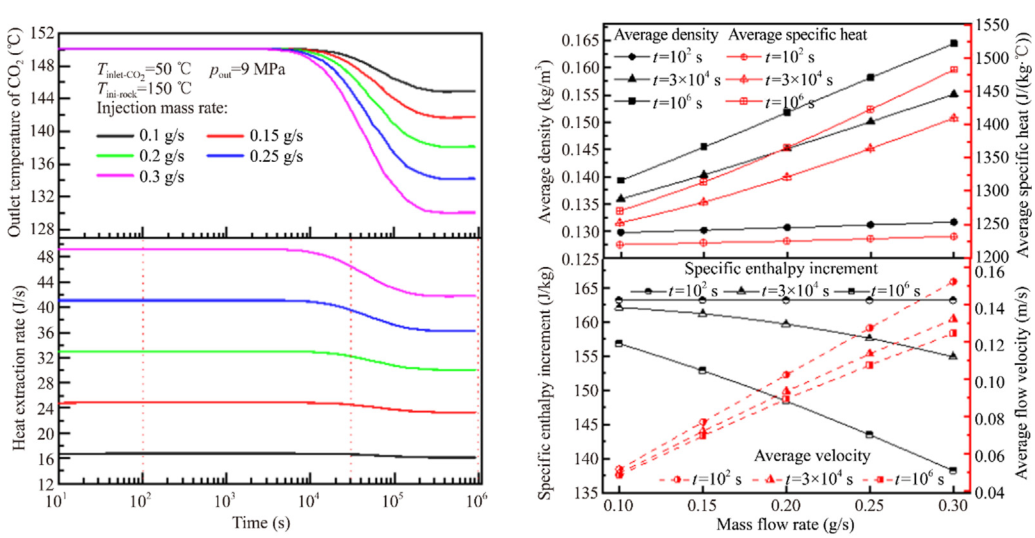

(a) Variation of outlet temperature and heat extraction rate with time

(b) Specific enthalpy increment and average flow rate of CO_2 at different time in fracture

Fig. 11. Modeling results for different mass flow rates.

4.4. Evaluation of heat extraction characteristics

It is apparent from Fig. 7 that both the fracture deformation and thermodynamic properties of the effluent CO_2 vary with heat transfer between the hot rock and injected cool fluid. Fig. 12 presents a conceptualization of the entire evolution processe of fracture deformation and heat production. At the initiation of CO_2 injection, the influent CO_2 is rapidly heated to the initial rock temperature. Decreasing effective stress-induced fracture-dilatancy dominates over the thermal-deformation. Under this condition, the CO_2-rock system is under an initial thermal equilibrium. The following influent CO_2 then first cools the asperities in the fracture, which reduces the fracture aperture and reduces heat production. Following this, due to CO_2 continuously absorbing heat from the rock matrix, the spatial temperature gradient in the matrix begins to gradually propagate from the fracture surface to the interior matrix, and concurrently progresses from the inlet to the outlet. The cooled matrix adjacent to the fracture accordingly shrinks, causing the fracture to reopen. Meanwhile, the heat production continues to fall as a result of the reduction in fracture-matrix temperature. During this stage, the rock permeability is controlled by the interaction between the fracture narrowing/opening and the matrix shrinkage [63]. Both mass flows of the CO_2 and heat extraction are dynamic. When the temperature difference between the rock and CO_2 is negligible, both the rock deformation and heat production of CO_2 are in a state of global thermal equilibrium. To evaluate the heat extraction through the CO_2 flux between the initial and global thermal equilibrium states, heat increments per unit mass of CO_2 are evaluated by independently varying the outlet pressure (Fig. 13a), mass flow rate (Fig. 13b) and inlet temperature of the CO_2 (Fig. 13c). In all instances, the heat increment recovered by the CO_2 in the state of initial thermal equilibrium is higher than that under the global thermal equilibrium. Indeed, both the initial temperature and the mass flow rate of CO_2 are negatively correlated to its heat increments. In contrast, raising the outlet pressure can increase the increment of heat recovery. Different from the incremental heat recovery of $scCO_2$, only increasing the initial temperature of the CO_2 can raise its outlet temperature, while increasing mass flow rate and the outlet pressure can reduce the outlet temperature of CO_2.

Heat extraction capacity by CO_2 is qualitatively analyzed by indexing against a single operational parameter relative to other specific conditions. In order to assess the influences among the three independent variables on the heat extraction and outlet (production) temperature of CO_2, a multi-linear regression is employed. The standard partial regression coefficient (β) and the R-squared values under the two equilibrium states are summarized in Tables 3 and 4, respectively. It is apparent that the R^2 values for both states exceed 0.98, indicating a high degree of fit.

Under the state of initial thermal equilibrium, it can be speculated, from the value of β (in Table 3), that the heat increment is positively correlated to the CO_2 outlet pressure, in contrast to its initial temperature. In addition, the mass flow rate of CO_2 has less impact on its heat increment. These results are in good agreement with the profiles in Fig. 13. In this case, when different controlling conditions are considered, varying initial temperature can significantly impact heat production.

According to the value of β in Table 4, the outlet pressure has a positive effect on the heat increment per unit mass of CO_2, while both the initial temperature and mass flow rate are negatively correlated. Conversely, the mass flow rate and outlet pressure are negatively correlated with outlet temperature, different from the inlet temperature being positively correlated. By comparing values of β in the two dependent variables, it can be concluded that the initial temperature of CO_2 has the greatest influence on heat production.

5. Conclusions

We complete an analysis of flow of supercritical CO_2 ($scCO_2$) within fractured hot rock as a prototypical geometry of an enhanced geothermal system (EGS) in hot and nominally dry rock (HDR).

(1) A rough-walled fracture in hot rock is simplified as an equivalent porous medium, where $scCO_2$ flow is governed by the Forchheimer equation and its thermal-physical properties are represented by the Span-Wagner model.

(2) During the continuous injection of $scCO_2$ into the hot rock, the rock permeability responds to, and is related to, interaction between the fracture narrowing/opening and matrix shrinkage. The fracture aperture decreases after initially increasing, then increases again towards a stable value. The fracture aperture increase at early time is attributed to

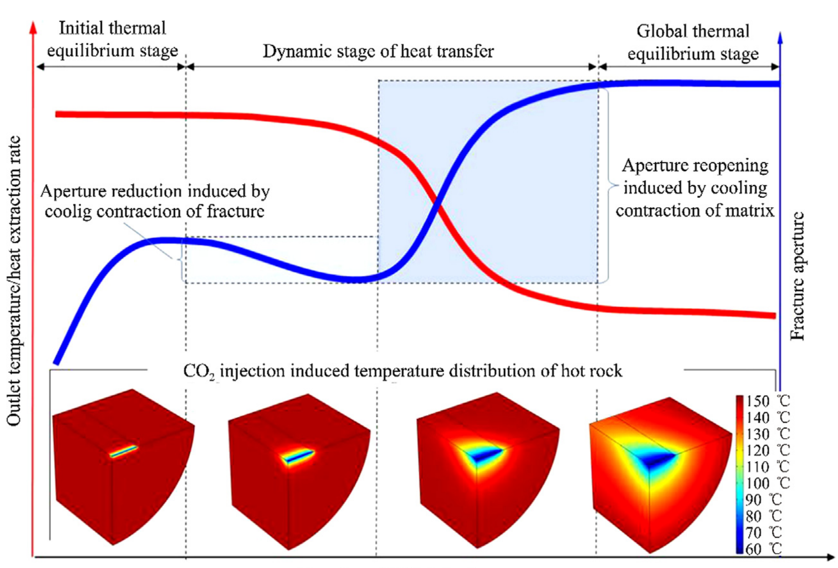

Fig. 12. Schematic describing the evolution of fracture aperture and heat extraction with the duration of $scCO_2$ injection.

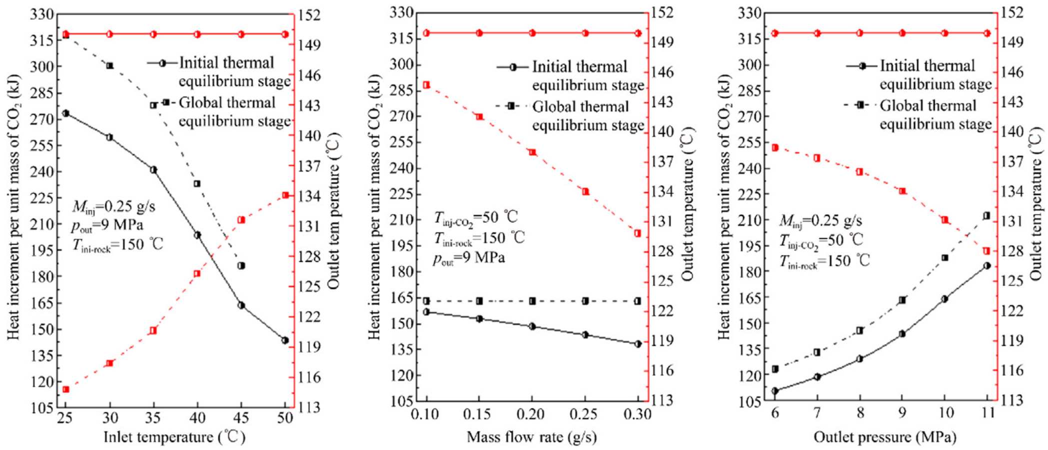

Fig. 13. Heat increment per unit mass of CO_2 and outlet temperature under where temperature, mass flow rate and outlet pressure are independently varied.

Table 3
Multiple linear regression analysis of CO_2-rock heat exchange under initial thermal equilibrium.

β	Injection mass flow rate	Outlet pressure	Inlet temperature	R^2
Heat increment per unit mass	0.017 ($p > 0.05$)	0.390	−0.875	0.984

Table 4
Multiple linear regression analysis of CO_2-rock heat exchange under global thermal equilibrium.

β	Injection mass flow rate	Outlet pressure	Inlet temperature	R^2
Heat increment per unit mass	0.483	0.368	−0.688	0.982
Outlet temperature	0.502	0.307	−0.704	0.986

Notes: β and R^2 results of multiple regression analysis are given in Tables 3 and 4. β is the standard partial regression coefficient and its absolute value measures the contribution of the independent variables to the dependent variables, indicating their respective importance in the linear multiple regression equation; R^2 is the coefficient of determination, an index of the goodness of fit of the regression model with R^2 = 1 representing a perfect fit.

the increase in CO_2 pressure. The following fracture closure results from the cooling and shrinkage of the rough surfaces of the fracture asperities in contact. The subsequent fracture reopening over the long term also results from cooling and contraction of the rock matrix near the fracture.

(3) Controls on heat extraction effected by the $scCO_2$ flux in the hot rock are evaluated by constructing a prototypical fracture-$scCO_2$ circulation model representative of a mid-sized portion of a reservoir containing a component single fracture. This model is exercised by separately and independently controlling injection fluid pressure, mass flow rate and initial temperature of CO_2, respectively. The heat extraction rate of the $scCO_2$ is shown to be positively corrrelated to its pore pressure. This is because both specific heat and density of $scCO_2$ are significantly increased with fluid pressure. Increasing the mass flow rate of $scCO_2$ also increases the heat extraction rate. When the initial temperature of the $scCO_2$ is below its pseudo-critical temperature, the heat extraction rate of $scCO_2$ is significantly improved.

(4) According to the outlet temperature profile of CO_2 with time, the heat transfer process between rock and CO_2 reflects both a short-term initial equilibrium state and a longer-term global equilibrium. Both heat increments per unit mass of CO_2 transmitted and outlet temperatures under the two equilibrium states are evaluated by separately and independently varying injection conditions of outlet pressure, then mass flow rate, then initial temperature. Under conditions of initial thermal equilibrium, the heat increment is higher than when a global thermal equilibrium is reached. Both the initial temperature and the mass flow rate of $scCO_2$ are negatively correlated to the heat increments, different from the effects of the outlet pressure. Only increasing the initial temperature of the $scCO_2$ can raise its outlet temperature, while increasing mass flow rate and the outlet pressure can reduce the outlet temperature of the $scCO_2$. A multi-linear regression analysis for the three $scCO_2$ injection scenarios, above, reveals that the thermal efficiency of $scCO_2$ is improved by varying the initial temperature of CO_2.

Acknowledgements

The financial support from the National Natural Science Foundation of China (Nos. 41772154 and 42102338), Natural Science Foundation of Shandong Province (Nos. ZR2019MA009 and ZR2020QE115), and SDUST Research Fund of China (No. 2018TDJH102) are all gratefully acknowledged.

References

[1] Shortall R, Davidsdottir B, Axelsson G. Geothermal energy for sustainable development: A review of sustainability impacts and assessment frameworks. Renew Sustain Energy Rev 2015;44:391–406.
[2] Pan SY, Gao M, Shah KJ, Zheng J, Pei SL, Chiang PC. Establishment of enhanced geothermal energy utilization plans: Barriers andstrategies. Renew Energy 2019;132:19–32.
[3] Wu XG, Huang ZW, Dai XW, Song HY, Zhang SK. Thermo-coupled FSI analysis of LN2 jet impinging on hot dry rock. Appl Therm Eng 2020;165:114621.

[4] Cui GD, Ren SR, Zhang L, Ezekiel J, Enechukwu C, Wang Y, Zhang R. Geothermal exploitation from hot dry rocks via recycling heat transmission fluid in a horizontal well. Energy 2017;128:366–77.
[5] Wei X, Feng ZJ, Zhao YS. Numerical simulation of thermo-hydromechanical coupling effect in mining fault-mode hot dry rock geothermal energy. Renew Energy 2019;139:120–35.
[6] Olasolo P, Juárez MC, Morales MP, ÐAmico S, Liarte IA. Enhanced geothermal systems (EGS): a review. Renew Sustain Energy Rev 2016;56:133–44.
[7] Olasolo P, Juárez MC, Olasolo J, Morales MP, Valdani D. Economic analysis of enhanced geothermal systems (EGS). a review of software packages for estimating and simulating costs. Appl Therm Eng 2016;104:647–58.
[8] Zhang W, Wang CG, Guo TK, He JY, Zhang L, Chen SJ, Qu ZQ. Study on the cracking mechanism of hydraulic and supercritical CO2 fracturing in hot dry rock under thermal stress. Energy 2021;221:119886.
[9] Xu RN, Zhang L, Zhang FZ, Jiang PX. A review on heat transfer and energy conversion in the Enhanced Geothermal Systems with water/CO_2 as working fluid. Int J Energy Res 2015;39:1722–41.
[10] Brown DW. A hot dry rock geothermal energy concept utilizing supercritical CO_2 instead of water. In Proceedings of Twenty-Fifth Workshop on Geothermal Reservoir Engineering. Stanford University, Stanford, California, USA; 2000.
[11] Pan C, Chávez O, Romero CE, Levy EK, Aguilar Corona A, Rubio-Maya C. Heat mining assessment for geothermal reservoirs in Mexico using supercritical CO_2 injection. Energy 2016;102:148–60.
[12] Zhang L, Jiang P, Wang Z, Xu R. Convective heat transfer of supercritical CO2 in a rock fracture for enhanced geothermal systems. Appl Therm Eng 2017;115:923–36.
[13] Luo J, Zhu YQ, Guo QH, Tan L, Zhuang YQ, Liu ML, Zhang CH, Xiang W, Rohn J. Experimental investigation of the hydraulic and heat transfer properties of artificially fractured granite. Sci Rep 2017;7(1).
[14] Luo J, Qi Y, Zhao Q, Tan L, Xiang W, Rohn J. Investigation of flow and heat transfer characteristics in fractured granite. Energies 2018;11(5):1228.
[15] Shaik AR, Rahman SS, Tran NH, Tran T. Numerical simulation of fluid-Rock coupling heat transfer in naturally fractured geothermal system. Appl Therm Eng 2011;31(10):1600–6.
[16] Zhang L, Luo F, Xu RN, Jiang PX, Liu HH. Heat transfer and fluid transport of supercritical CO_2 in enhanced geothermal systems with local thermal nonequilibrium model. Energy Procedia 2014;63:7644–50.
[17] Zhao Z. On the heat transfer coefficient between rock fracture walls and flowing fluid. Comput Geotech 2014;59:105–11.
[18] Zhao J. Experimental Studies of the Hydro-Thermo-Mechanical Behaviour of Joints in Granite. Doctoral dissertation. London: Imperial College; 1987, p. 273.
[19] Zhao J. Geothermal testing and measurements of rock and rock fractures. Geothermics 1994;23(3):215–31.
[20] Huang Y, Zhang Y, Yu Z, Ma Y, Zhang C. Experimental investigation of seepage and heat transfer in rough fractures for enhanced geothermal systems. Renew Energy 2019;135:846–55.
[21] Li ZW, Feng XT, Zhang YJ, Zhang C, Xu TF, Wang YS. Experimental research on the convection heat transfer characteristics of distilled water in manmade smooth and rough rock fractures. Energy 2017;133:206–18.
[22] Bai B, He YY, Li XC, Hu SB, Huang XX, Li J, Zhu JL. Local heat transfer characteristics of water flowing through a single fracture within a cylindrical granite specimen. Environ Earth Sci 2016;75(22):1460.
[23] Ma Y, Zhang Y, Hu Z, Yu Z, Huang Y, Zhang C. Experimental study of the heat transfer by water in rough fractures and the effect of fracture surface roughness on the heat transfer characteristics. Geothermics 2019;81:235–42.
[24] Huang X, Zhu J, Li J, Bai B, Zhang G. Fluid friction and heat transfer through a single rough fracture in granitic rock under confining pressure. Int Commun Heat Mass Transfer 2016;75:78–85.
[25] Wang CG, Liu SQ, Shi XK, Cui GL, Wang HX, Jin X, Fan K, Hu S. Numerical modeling of contaminant advection impact on hydrodynamic diffusion in a deformable medium. J Rock Mech Geotech Eng 2021.
[26] Heinze T, Hamidi S, Galvan B. A dynamic heat transfer coefficient between fractured rock and flowing fluid. Geothermics 2017;65:10–6.
[27] Pruess K. Enhanced geothermal systems (EGS) using CO_2 as working fluid-A novel approach for generating renewable energy with simultaneous sequestration of carbon. Geothermics 2006;35(4):351–67.
[28] Hu JJ, Xie HP, Sun Q, Li CB, Liu GK. Changes in the thermodynamic properties of alkaline granite after cyclic quenching following high temperature action. Int J Min Sci Technol 2021;31(5):843–52.
[29] Zhang W, Guo TK, Qu ZQ, Wang Z. Research of fracture initiation and propagation in HDR fracturing under thermal stress from meso-damage perspective. Energy 2019;178:508–21.
[30] Gelet R, Loret B, Khalili N. Thermal recovery from a fractured medium in local thermal non-equilibrium. Int J Numer Anal Met 2013;37:2471–501.
[31] Chen JL, Jiang FM. Designing multi-well layout for enhanced geothermal system to better exploit hot dry rock geothermal energy. Renew Energ 2015;74:37–48.
[32] Kolditz O, Clauser C. Numerical simulation of flow and heat transfer in fractured crystalline rocks: application to the hot dry rock site in Rosemanowes (U.K.). Geothermics 1998;27(1):1–23.
[33] Fox DB, Sutter D, Beckers KF, Lukawski MZ, Koch DL, Anderson BJ, Tester JW. Sustainable heat farming: modeling extraction and recovery in discretely fractured geothermal reservoirs. Geothermics 2013;46:42–54.
[34] Ekneligoda TC, Min K. Determination of optimum parameters of doublet system in a horizontally fractured geothermal reservoir. Renew Energ 2014;65:152–60.
[35] Bai M, Roegiers JC. Fluid flow and heat flow in deformable fractured porous media. Int J Eng Sci 1994;32(10):1615–33.
[36] Luo J, Zhu YQ, Guo QH, Tan L, Zhuang YQ, Liu ML, Zhang CH, Xiang W, Rohn J. Experimental investigation of the hydraulic and heat-transfer properties of artificially fractured granite. Sci Rep 2017;7(1).
[37] Kamali-Asl A, Ghazanfari E, Perdrial N, Bredice N. Experimental study of fracture response in granite specimens subjected to hydrothermal conditions relevant for enhanced geothermal systems. Geothermics 2018;72:205–24.
[38] Morrow CA, Moore DE, Lockner DA. Permeability reduction in granite under hydrothermal conditions. J Geophys Res Solid Earth 2001;106(B12):30551–60.
[39] Wang S, Huang Z, Wu YS, Winterfeld PH, Zerpa LE. A semi-analytical correlation of thermal-hydraulic-mechanical behavior of fractures and its application to modeling reservoir scale cold water injection problems in enhanced geothermal reservoirs. Geothermics 2016;64:81–95.
[40] Kohl T, Evansi KF, Hopkirk RJ, Rybach L. Coupled hydraulic, thermal and mechanical considerations for the simulation of hot dry rock reservoirs. Geothermics 1995;24(3):345–59.
[41] Zhao Y, Feng Z, Feng Z, Yang D, Liang W. THM (Thermo-hydro-mechanical) coupled mathematical model of fractured media and numerical simulation of a 3D enhanced geothermal system at 573 K and buried depth 6000–7000 M. Energy 2015;82:193–205.
[42] Wang CG, Zhang JD, Zang YX, Zhong RZ, Wang JG, Wu Y, Jiang YJ, Chen ZW. Time-dependent coal permeability: Impact of gas transport from coal cleats to matrices. J Nat Gas Sci Eng 2021;88:103806.
[43] Wang G, Qin XJ, Han DY, Liu ZY. Study on seepage and deformation characteristics of coal microstructure by 3D reconstruction of CT images at high temperatures. Int J Min Sci Technol 2021;31(2):175–85.
[44] Zhang BY, He QY, Lin ZB, Li ZH. Experimental study on the flow behaviour of water-sand mixtures in fractured rock specimens. Int J Min Sci Technol 2021;31(3):377–85.
[45] Hicks TW, Pine RJ, Willis-Richards J, Xu S, Jupe AJ, Rodrigues NEV. A hydro-thermo-mechanical numerical model for HDR geothermal reservoir evaluation. Int J Rock Mech Min Sci Geomech Abstr 1996;33(5):499–511.
[46] Pandey SN, Vishal V. Sensitivity analysis of coupled processes and parameters on the performance of enhanced geothermal systems. Sci Rep 2017;7:17057.
[47] Su CD, Qiu JD, Wu QH, Weng L. Effects of high temperature on the microstructure and mechanical behavior of hard coal. Int J Min Sci Technol 2020;30(5):643–50.
[48] Wu Y, Tao J, Wang JH, Zhang Y, Peng SH. Experimental investigation of shale breakdown pressure under liquid nitrogen pre-conditioning before nitrogen fracturing. Int J Min Sci Technol 2021;31(4):611–20.
[49] Zinsalo JM, Lamarche L, Raymond J. Injection strategies in an enhanced geothermal system based on discrete fractures model. Appl Therm Eng 2020;169:114812.
[50] Wu B, Zhang Xi, Jeffrey RG, Bunger AP, Jia S. A simplified model for heat extraction by circulating fluid through a closed-loop multiple-fracture enhanced geothermal system. Appl Energy 2016;183:1664–81.
[51] Magliocco MJ, Glaser SD, Kneafsey TJ. Laboratory and Numerical Studies of Heat Extraction from Hot Porous Media by Means of Supercritical CO_2. Transp Porous Media 2015;108(1):85–104.
[52] Sun FR, Yao YD, Chen MQ, Li XF, Zhao L, Meng Y, Sun Z, Zhang T, Feng D. Performance analysis of superheated steam injection for heavy oil recovery and modeling of wellbore heat efficiency. Energy 2017;125:795–804.
[53] Song WQ, Wang CG, Du YK, Shen BT, Chen SJ, Jiang YJ. Comparative analysis on the heat transfer efficiency of supercritical CO_2 and H_2O in the production well of enhanced geothermal system[J]. Energy 2020;205:118071.
[54] Sun FR, Yao YD, Li GZ, Li XF. Geothermal energy development by circulating CO*2* in a U-shaped closed loop geothermal system. Energy Convers Manage 2018;174:971–82.
[55] Span R, Wagner W. A new equation of state for carbon dioxide covering the fluid region from the triple-toint temperature to 1100 K at pressures up to 800 MPa. J Phys Chem Ref Data 1996;25(6):1509–96.
[56] Wu Y, Li P. The potential of coupled carbon storage and geothermal extraction in a CO_2-enhanced geothermal system: a review. Geothermal Energy 2020;8:19.
[57] Witherspoon PA, Wang JSY, Iwai K, Gale JE. Validity of Cubic Law for fluid flow in a deformable rock fracture. Water Resour Res 1980;16(6):1016–24.
[58] Detournay E, Cheng HD. Fundamentals of poroelasticity. Anal Des Methods 1993;140(1):113–71.
[59] Cui GL, Feng XT, Pan ZJ, Chen TY, Liu JS, Elsworth D, Wang CG. Impact of shale matrix mechanical interactions on gas transport during production. J Petrol Sci Eng 2020;184:106524.
[60] Pandey SN, Vishal V, Chaudhuri A. Geothermal reservoir modeling in a coupled thermo-hydro-mechanical- chemical approach: a review. Earth Sci Rev 2018;185:1157–69.
[61] National Institute of Standards and Technology. Isothermal Properties for Carbon dioxide; 2018. https://webbook.nist.gov.
[62] Fenghour A, Wakeham WA, Vesovic V. The Viscosity of Carbon Dioxide. J Phys Chem Ref Data 1998;27(1):31–44.
[63] Vesovic V, Wakeham WA, Olchowy GA, Sengers JV, Watson JTR, Millat J. The transport properties of carbon dioxide. J Phys Chem Ref Data 1990;19 (3):763–808.
[64] Jiang P, Zhang L, Xu R. Experimental study of convective heat transfer of carbon dioxide at supercritical pressures in a horizontal rock fracture and its application to enhanced geothermal systems. Appl Therm Eng 2017;117:39–49.

[65] Zhang W, Qu Z, Guo T, Wang Z. Study of the enhanced geothermal system (EGS) heat mining from variably fractured hot dry rock under thermal stress. Renew Energy 2019;143:855–71.
[66] Sun ZX, Zhang X, Xu Y, Yao J, Wang HX, Lv SH, Sun ZL, Huang Y, Cai MY, Huang XX. Numerical simulation of the heat extraction in EGS with thermal-hydraulic-mechanical coupling method based on discrete fractures model. Energy 2017;120:20–33.
[67] Chen Y, Zhao Z. Heat transfer in a 3D rough rock fracture with heterogeneous apertures. Int J Rock Mech Min Sci 2020;134:104445.
[68] Sun FR, Yao YD, Li GZ, Li XF. Geothermal energy extraction in CO_2 rich basin using abandoned horizontal wells. Energy 2018;158:760–73.
[69] Sun FR, Yao YD, Li GZ, Li XF. Performance of geothermal energy extraction in a horizontal well by using CO_2 as the working fluid. Energy Convers Manage 2018;171:1529–39.